

MoD-ART: Modal Decomposition of Acoustic Radiance Transfer

Matteo Scerbo*, Sebastian J. Schlecht†, Randall Ali*, Lauri Savioja‡, Enzo De Sena*

*Institute of Sound Recording, University of Surrey, Guildford, UK

m.scerbo, r.ali, e.desena@surrey.ac.uk

†Multimedia Communications and Signal Processing, University of Erlangen-Nuremberg, Germany

sebastian.schlecht@fau.de

‡Department of Computer Science and Acoustics Lab, Aalto University, Espoo, Finland

lauri.savioja@aalto.fi

Abstract—Modeling late reverberation at interactive speeds is a challenging task when multiple sound sources and listeners are present in the same environment. This is especially problematic when the environment is geometrically complex and/or features uneven energy absorption (e.g. coupled volumes), because in such cases the late reverberation is dependent on the sound sources’ and listeners’ positions, and therefore must be adapted to their movements in real time. We present a novel approach to the task, named modal decomposition of Acoustic Radiance Transfer (MoD-ART), which can handle highly complex scenarios with efficiency. The approach is based on the geometrical acoustics method of Acoustic Radiance Transfer, from which we extract a set of energy decay modes and their positional relationships with sources and listeners. In this paper, we describe the physical and mathematical meaningfulness of MoD-ART, highlighting its advantages and applicability to different scenarios. Through an analysis of the method’s computational complexity, we show that it compares very favourably with ray-tracing. We also present simulation results showing that MoD-ART can capture multiple decay slopes and flutter echoes.

Index Terms—Room acoustics modeling, Acoustic Radiance Transfer, Modal decomposition, Common Slopes model.

I. INTRODUCTION

The efficient prediction of late reverberation poses a considerable challenge in the field of room acoustics modeling, as it requires high reflection orders and accurate modeling of diffuse reflections. This endeavour is relevant in video game sound design, as well as any augmented reality (AR) or virtual reality (VR) application, where plausible auralization greatly enhances the sense of immersion [2] and must be performed at interactive speeds. Of particular interest are environments which can show different energy decay behaviours depending on the positions of sound sources and listeners, in which case the interactive adaptation of reverberation is all the more important and challenging. A classic example is that of coupled volumes, where rooms possessing different reverberation properties are connected by a series of apertures, and sources/listeners may be located in different rooms.

This work was supported by the Engineering and Physical Sciences Research Council under the Scalable Room Acoustics Modelling Grant EP/V002554/1. R. Ali is a voluntary research associate at KU Leuven, Belgium and has been supported by the FWO Research Project G0A0424N.

Part of this work was presented at the 27th International Conference on Digital Audio Effects (DAFx24) [1].

The strict requirements of interactive late reverberation prediction make many room acoustic models unsuitable for the task. Wave-based methods such as finite-difference time-domain (FDTD) [3], finite element method (FEM) [4], and boundary element method (BEM) [5] are very computationally expensive, especially for late reverberation (i.e. broadband responses of long duration), making them difficult to use at interactive speeds [6]. The same goes for the Image Source Method (ISM) [7], which becomes prohibitively complex for very high reflection orders, especially in nonconvex environments [8]. Methods like beam-tracing scale better in terms of computational complexity [9], [10], but they still cannot model diffuse reflections, which become predominant in late reverberation [11, p. 125]. The Ray Tracing Method (RTM) is better suited for late reverberation [12], modeling scattering through stochastic sampling of diffuse reflections [13] – although this requires high numbers of rays to model complex scenes reliably, which is problematic for real-time applications [14]. Another drawback of the RTM is that, any time a sound source or listener moves, a new simulation needs to be run “from scratch”. Acoustic Radiance Transfer (ART) and the Acoustic Diffusion Equation (ADE), on the other hand, enable the precomputation of the most important parameters for energy propagation in the environment [15], [16], which do not depend on the positions of sources and listeners. This alleviates the computational load at runtime, particularly in multiple-input, multiple-output (MIMO) scenarios (i.e. more than one sound source and/or listener in the same environment), because the movement of individual sources/listeners only requires minimal updates of model parameters. In fact, ART can be run in real time with interactive positional updates [17].

We propose an approach for late reverberation prediction, the *modal decomposition of Acoustic Radiance Transfer (MoD-ART)*, which offers the advantages of ART, but with much lower computational requirements (operations and memory). Our approach is built on the observation that ART (in particular, Time-Domain Acoustic Radiance Transfer (TD-ART) [18]) is a recursive linear time-invariant (LTI) system, which can be expressed by its modal decomposition [19]. The outcome of the decomposition is a set of eigenvalues and eigenvectors, which respectively describe the modes’ position-independent behaviour and their “coupling” with source and

arXiv:2412.04534v1 [cs.SD] 5 Dec 2024

listener positions [20]. As previously mentioned, in ART there is a separation between the interactive elements and the parameters characterising energy propagation in the environment. This separation is leveraged by the modal decomposition, such that the eigenvalues are representative of the environment’s energy decay modes – which are independent of sound sources and listeners [21], [22]. What differentiates MoD-ART from modal analyses such as [20], [21] is that the physical interpretations in [20], [21] deal with pressure signals and find room modes, whereas MoD-ART deals with energy signals and finds energy decay modes.

The groundwork for MoD-ART was previously established in [1], and the approach is expanded upon here. In this paper we present a thorough discussion of the connections between MoD-ART parameters and physical aspects of the modeled scene; we offer insight in the multiple possible applications of MoD-ART, and analyse its computational requirements with respect to RTM and TD-ART. The efficiency of the proposed approach is attributed to two principles, both discussed in this paper: 1) a small number of energy modes is sufficient to capture all desired aspects of late reverberation, 2) interactive elements (i.e. sources, listeners) do not alter the most fundamental parameters of ART. We present the reasoning behind both of these points, as well as their implications for the computational requirements of MoD-ART and for its applicability in different scenarios.

The remainder of the paper is organized as follows. Section II gives an overview of echograms, TD-ART, its interpretation as an LTI system, and its modal decomposition. Section III discusses the physical significance of the decomposition, the rationale behind the proposed method, and some practical aspects of the approach. Section IV analyzes the method’s computational complexity, with a particular focus on interactive operation. Section V presents some simulation results which illustrate different aspects and properties of the proposed method, and validate its accuracy. Section VI concludes the paper with a summary and some final remarks.

II. BACKGROUND

The room impulse response (RIR) is a signal which entirely characterizes the propagation of sound from a given source to a given listener in a room [11]. Any anechoic sound signal (i.e. one recorded in a non-reverberant environment) may be *auralized* by convolution with the RIR, which produces the same result as if the sound had been recorded in the scenario the RIR describes. The echogram, or energy response, corresponds to the square of the RIR [11]. When it comes to late reverberation in particular, the sign of the RIR (lost when taking the square) holds little perceptual relevance, and modeling the echogram is sufficient for plausible auralization [23]. For this reason, it is commonplace to use an energy-based geometrical acoustics (GA) model such as RTM to produce an echogram, and then to retrieve a RIR to be used in convolution by introducing stochastic sign information [24]. In this process, known as *noise-shaping*, the echogram provides the low-varying energy behaviour while the stochastic process provides sample-by-sample fluctuations – as such, the echogram may be evaluated at a much lower sample rate than the one used for

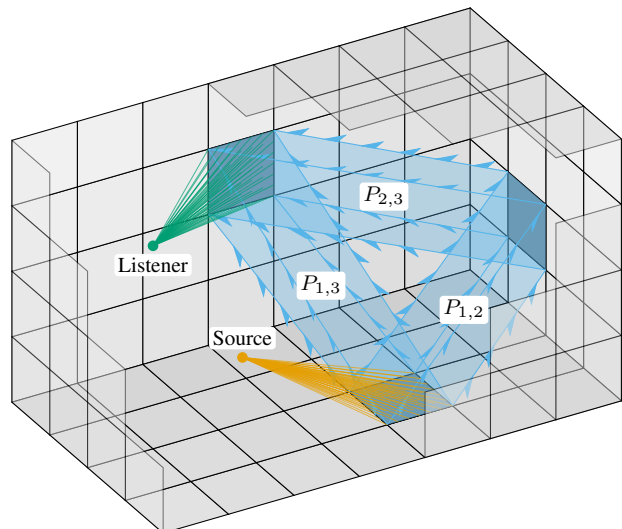


Fig. 1: Illustration of three volumetric paths. In total, there are two volumetric paths connecting each pair of patches with an unobstructed view of each other (one path in each direction). The paths in this figure go from patch 1 to patch 2 ($P_{1,2}$), from 1 to 3 ($P_{1,3}$), and from 2 to 3 ($P_{2,3}$). The figure also shows a sound source and a listener, respectively supplementing and detecting the energy contained by the volumetric paths.

auralization [11, p. 320]. Noise-shaping is usually performed separately for different frequency bands, employing band-passed stochastic signals and different echograms [24].

A. Acoustic Radiance Transfer

Acoustic Radiance Transfer (ART) is a GA model that characterizes acoustic energy as propagating over a discrete set of “volumetric paths” in the environment. It is based on the assumption that energy is diffuse and uniform within each path [15], making it particularly suitable to model late reverberation (reverberant energy gradually becomes diffuse over time [11]). Some examples of volumetric paths are illustrated in Fig. 1: they connect pairs of surface patches, and they are orientation-sensitive. Also illustrated in Fig. 1 are a sound source and a listener; their interaction with volumetric paths is explained later in this same section.

The method proposed in this paper is derived starting from Time-Domain Acoustic Radiance Transfer (TD-ART), an implementation of ART which produces the desired echogram by iteratively propagating the volumetric paths’ energy over (discrete) time [18]. The MIMO TD-ART model can be expressed in the z -domain as

$$\mathbf{s}(z) = \mathbf{A}T_a(z)\mathbf{s}(z) + \mathbf{B}(z)\mathbf{x}(z), \quad (1a)$$

$$\mathbf{y}(z) = \mathbf{C}(z)\mathbf{s}(z) + \mathbf{D}(z)\mathbf{x}(z), \quad (1b)$$

where $\mathbf{x}(z) \in \mathbb{C}^{S \times 1}$ are the input energy signals (with S sound sources), $\mathbf{y}(z) \in \mathbb{C}^{L \times 1}$ are the output energy signals (with L listeners), $\mathbf{s}(z) \in \mathbb{C}^{N \times 1}$ are the energy signals traversing each of the N volumetric paths, and the remaining parameters \mathbf{A} , $T_a(z)$, $\mathbf{B}(z)$, $\mathbf{C}(z)$, and $\mathbf{D}(z)$ are defined in the following. The block diagram form of this system is presented in Fig. 2.

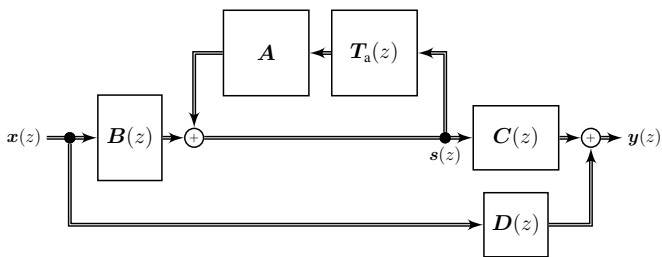


Fig. 2: Block diagram of a TD-ART model, as expressed in (1). The filters in $B(z)$ describe how the input energy $x(z)$ is distributed among the volumetric paths, and the filters $C(z)$ describe how the volumetric paths' energy $s(z)$ is gathered into the energy outputs $y(z)$. The delays $T_a(z)$ model the propagation of energy along each volumetric path, and the matrix A describes how energy is reflected/scattered from each path to the others. The filters $D(z)$ model the direct energy propagation between sources and listeners.

The matrices $A \in \mathbb{R}^{N \times N}$ and $T_a(z) \in \mathbb{C}^{N \times N}$ govern the recursive energy propagation in the modeled environment. The first, A , describes energy reflection and diffusion among the paths; it encodes the information on the surface patches' absorption and scattering coefficients, as well as the form factors relating pairs of patches¹. The second, $T_a(z)$, is a diagonal matrix of filters applying delay and (optionally) temporal spreading [18], modeling propagation along the related path. The filters forming the diagonal of $T_a(z)$ may also apply air absorption. The operation $AT_a(z)s(z)$ in (1a) models the energy being propagated and attenuated along each path, then reflected and mixed into the same set of paths.

The matrix $B(z) \in \mathbb{C}^{N \times S}$ describes the amount of energy provided by each sound source to each propagation path, as well as the propagation delays from the source positions to the paths themselves. In a similar fashion, $C(z) \in \mathbb{C}^{L \times N}$ describes the attenuation and delay with which energy is picked up by listeners. Both $B(z)$ and $C(z)$ are evaluated with a single order of ray-tracing, by tracing rays from each sound source and listener position and determining the volumetric path that each ray falls into. Lastly, $D(z) \in \mathbb{C}^{L \times S}$ models the line-of-sight component between each sound source and listener, since this would not otherwise be modeled by A and $T_a(z)$.

Note the separation of components which depend on sound source positions (i.e. B , D), listener positions (i.e. C , D), or neither (i.e. A , T_a). If a single sound source or listener changes position, only the parameters related to the moving entity need to be updated before running the filter. This aspect comes into play in the development of our proposed method. It is particularly advantageous in MIMO and/or interactive scenarios, as discussed further in Section IV-C.

The TD-ART model may also be represented in state-space form (presented in Appendix A) or in transfer function form:

$$E(z) = C(z) [I - AT_a(z)]^{-1} B(z) + D(z). \quad (2)$$

¹Also known as shape factors or view factors, these are the primary descriptors of radiance transfer [25, p. 38]. They can be interpreted as the surface patches' relative "view" of each other, or the "aperture" of the volumetric propagation paths.

This transfer function is the z -transform of the modeled echogram $E[n]$. In the following section, we see how it can be expressed in terms of its modal decomposition.

B. Modal decomposition

The transfer function of any linear time-invariant (LTI) system can be expressed in terms of poles λ_m and residues R_m , for $m \in 1, \dots, M$, where M is the system order. The residues R_m have shape $L \times S$, like the transfer function itself – in the single-input, single-output (SISO) case, they are scalars. Through this decomposition, the transfer function takes the form of a sum of one-pole resonators [19]:

$$E(z) = D(z) + \sum_{m=1}^M \frac{R_m}{1 - \lambda_m z^{-1}}, \quad (3)$$

or, expressed in the time domain,

$$E[n] = D[n] + \sum_{m=1}^M R_m \lambda_m^n. \quad (4)$$

The system poles are also known as its eigenvalues.

Given the form of the TD-ART transfer function (2), the system poles are the roots of the polynomial

$$p(z) = \det(P(z)), \quad (5)$$

where $P(z) = I - AT_a(z)$ is the transfer function of the recursive loop. The residues are defined [26] as

$$R_m = \frac{C(\lambda_m) \text{adj}(P(\lambda_m)) B(\lambda_m)}{\text{tr}(\text{adj}(P(\lambda_m)) P'(\lambda_m))}, \quad (6)$$

where $\text{adj}(P) = P^{-1} \det(P)$ is the adjugate of P , $\text{tr}(P)$ is the trace of P , and

$$P'(z) = \frac{dP(z)}{dz} = -A \frac{dT_a(z)}{dz} = -AT_a'(z) \quad (7)$$

is the element-wise derivative of $P'(z)$. By definition of λ_m , we have that $P(\lambda_m)$ is singular, which in turn means its adjugate has rank one. As such, the adjugate can be expressed as an outer product of two vectors,

$$\text{adj}(P(\lambda_m)) = v_m w_m^H. \quad (8)$$

These two vectors are the left (w_m) and right (v_m) eigenvectors related to the eigenvalue λ_m , and they describe the mode's positional dependency. This is discussed in detail in the following section, alongside the significance of the modal decomposition in the context of TD-ART, and its usefulness for late reverberation modeling.

III. PROPOSED METHOD

Our proposed method, MoD-ART, is comprised of the following steps (elaborated over the remainder of this section):

- 1) (Offline) Evaluate non-interactive parameters: A , $T_a(z)$.
- 2) (Offline) Evaluate modal parameters: λ_m , v_m , w_m .
- 3) (Runtime) Evaluate interactive parameters: $B(z)$, $C(z)$.
- 4) (Runtime) Evaluate residues R_m .
- 5) (Runtime) Assemble the echogram as per (4).
- 6) (Runtime) Retrieve the RIR, convolve with source signals.

The true strength of MoD-ART lies in the fact that the modal decomposition is reduced to a very small subset of poles. The reason for this reduction stems from the physical significance of the modal parameters λ_m and \mathbf{R}_m , discussed in Section III-A. We propose two criteria for selecting the subset of poles, and present some adapted modal decomposition techniques in light of this, in Section III-B.

A. Physical significance of modal parameters

When ART is viewed from the standpoint of system theory, the system's impulse response is the modeled echogram. Here, it bears repeating that the echogram is the *square* of the RIR. The modal decomposition of the ART impulse response is not to be confused with the modal decomposition of the room impulse response. When the impulse response of ART is decomposed as in (4), each component

$$\mathbf{E}_m[n] = \mathbf{R}_m \lambda_m^n \quad (9)$$

characterizes a particular *energy decay mode* of the acoustic environment. In contrast, the individual components of the RIR's modal decomposition are room modes, related to the resonance frequencies of the environment (also known as eigenfrequencies). The individual components of the echogram's modal decomposition have very different interpretations, which are discussed in the following. Since the relationship between RIR and echogram (squared RIR) is nonlinear, there is no straight-forward connection between the modal decomposition of one or the other. In other words, in general, there is no one-to-one relationship between individual energy decay modes and individual room modes.

The first thing to note is that the form of (4) is quite similar to several parametric models which describe the decay of reverberation modes [16], [21], [22]. The temporal evolution of each mode (9), governed by the pole λ_m , is exclusively characterized by the recursion parameters \mathbf{A} and $\mathbf{T}_a(z)$. The residues \mathbf{R}_m , which depend on the input-output parameters $\mathbf{B}(z)$, $\mathbf{C}(z)$ in addition to \mathbf{A} , $\mathbf{T}_a(z)$, only apply scaling (they do not control the modes' temporal evolution). As discussed in the previous section, the recursion parameters only depend on characteristics of the acoustic environment itself – they are independent of the positions of sound sources and listeners. By extension, the same can then be said of the energy modes' temporal evolution, which is independent of the residues. This is also equivalent to the aforementioned parametric models, where modes' decay rates are independent of sources and listeners' positions, which in turn affect the modes' scaling.

Given their interpretation as energy quantities, all of the inputs, outputs, and state variables of ART only take nonnegative values. This makes ART a *positive linear system* [27], and several observations follow as consequence. For the purpose of the present work, the most important property of positive linear systems is given by the Frobenius theorem [27, Thm. 11]. It states that such systems always have one positive and real dominant eigenvalue λ_F , also known as Frobenius eigenvalue, such that $|\lambda_m| \leq |\lambda_F|, \forall m$. The theorem also states that, among the eigenvectors associated to λ_F , one is guaranteed to be positive – in other words, the residue associated to λ_F is

always positive. An intuitive interpretation of these statements can be gained by considering the limit

$$\lim_{n \rightarrow \infty} \mathbf{E}[n] = \lim_{n \rightarrow \infty} \sum_{m=1}^M \mathbf{R}_m \lambda_m^n = \mathbf{R}_F \lambda_F^n. \quad (10)$$

As the time index tends to infinity, the pole(s) with largest magnitude dominate all others. The response is entirely non-negative (again, because of its interpretation as an energy quantity) and therefore the dominant mode(s) must be as well. The remainder of this discussion is divided between the physical significance of pole values, and that of residue values.

1) *Physical significance of poles:* Since ART is a real-valued system (i.e. its impulse response, the echogram, is real-valued), complex poles always appear in conjugate pairs [19]. In general z -domain system analysis, poles lying on the real positive axis characterize non-oscillatory modes; pairs of complex poles characterize oscillatory modes; poles on the negative real axis characterize modes which oscillate at the Nyquist frequency [19]. Moreover, poles on the unit circle are “critically stable”, i.e. their modes do not increase nor decrease over time; poles with magnitude below 1 are stable (decay over time), and poles with magnitude above 1 are unstable (diverge over time). In the context of echogram decomposition, we can attribute physical significance to each of these behaviours.

Non-oscillatory energy decay modes are the primary concern for late reverberation. When reverberation is analyzed by using energy decay curves (EDCs), such modes appear as slopes (on a logarithmic scale). In simple spaces, the EDC generally follows a single slope [11, p. 97]; the reverberation time (T_{60}) is based on this. In the context of modal decomposition, said slope is related to the dominant pole λ_F (recall the intuition based on $\lim_{n \rightarrow \infty} \mathbf{E}[n]$). More complex environments, such as coupled volumes or spaces with uneven energy absorption, may present multiple decay slopes [11, Sec. 5.8]. Each slope is related to a real, positive pole (i.e. a non-oscillatory mode in the echogram decomposition), and the slope's reverberation time is related to the pole's magnitude by the following, derived in Appendix B:

$$T_{60}(\lambda_m) = \frac{1}{f_s} \frac{\ln 10^{-6}}{\ln |\lambda_m|}, \quad (11)$$

where f_s is the sample rate. This $T_{60}(\lambda_m)$ is also valid for oscillatory modes, where it is related to the mode's amplitude envelope [19]. If the echogram includes a constant noise floor term, it will appear in the decomposition as a real pole equal to 1: a non-oscillatory mode without decay. A similar interpretation is used in [22].

Oscillatory energy decay modes may take on multiple roles in the decomposition. In the early response, they model distinct reflections and other details of the echogram. In late reverberation, oscillatory modes may appear in cases where the echogram presents long-term oscillations such as flutter echoes. In Section V-B, we show an example where a flutter echo is characterized by a set of complex poles in the decomposition. The relationship between the phase of a

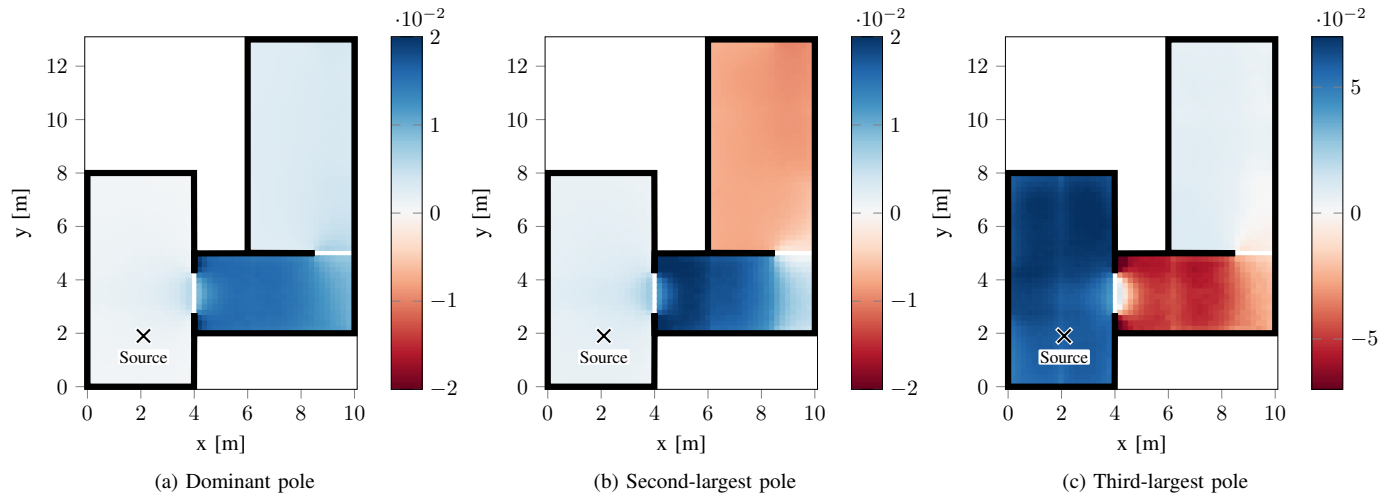


Fig. 3: Positional dependence of residues in a scene featuring three coupled rooms. The position of the sound source is fixed, and residues’ values are plotted as a function of the listener’s position. The three shown residues are those related to the poles with (a) largest, (b) second-largest, and (c) third-largest magnitudes, all of which are real and positive. Note that the three plots’ colorbars cover different ranges.

complex pole and the related mode’s frequency is the same as in general z -domain system analysis:

$$f(\lambda_m) = f_s \frac{\angle \lambda_m}{2\pi}. \quad (12)$$

Note that poles on the positive real axis correspond to zero-frequency modes, as expected.

2) *Physical significance of residues*: Residues related to real poles are themselves real, while residues related to complex poles may be complex. Just like for poles, residues’ role in the decomposition (and their physical interpretation) can be differentiated in terms of their magnitude and phase. Residues’ magnitudes simply weight the relative modes’ overall energy contribution. If \mathbf{R}_m has larger magnitude for one source-listener pair in particular, it means the m^{th} mode has a greater influence on the echogram for that particular pairing. For complex poles, residues’ phase has a similarly straight-forward interpretation, as it regulates the oscillatory modes’ starting phase. For real, positive poles, however, residues’ phase is deserving of further discussion. As previously mentioned, residues related to real poles are likewise real – but they may be negative, in which case the entire term (9) is negative. Negative modes detract energy from the decomposition, although the sum of all modes (the echogram) is always nonnegative. They occur in environments where the reverberation presents a fade-in period for some source-listener configurations [28]. Examples of this are presented in Section V-A.

The plots in Fig. 3 show how the value of three residues changes for different positions of a listener. The considered environment – which is also employed for the simulations illustrated in Section V-A – is composed of three rooms connected in sequence, with the middle room being the most reverberant. The maps in Fig. 3 are produced by fixing the sound source position (marked by an X) in the left-most room, and evaluating the residues for listeners positioned on a grid covering the entire space. The three shown residues are those

related to the three modes with poles of largest magnitude; all three poles are real and positive, and as such, their residues always take on real values. As predicted by the Frobenius theorem, the residue of the dominant pole (Fig. 3a) never takes negative values. The second and third modes’ residues (Fig. 3b, 3c), on the other hand, take on negative values in the right-most and middle rooms, respectively. This indicates that the second mode removes energy from the echogram when the listener is in the middle room, and the third mode does so when the listener is in the right-most room. Finally, note how the values taken by the third mode’s residue (Fig. 3c) reach larger magnitudes than the other two. This is because the third shown energy mode (the third-most reverberant in the decomposition) is related to the left-most room (the third-most reverberant in the scene). The sound source is placed in the left-most room, and stimulates the related energy mode with more strength than it does the other two modes. This manifests as the residue’s larger magnitude – recall that the residue’s magnitude controls the magnitude of the mode itself.

Combining (6), (7), and (8), residues take the form

$$\mathbf{R}_m = \frac{\mathbf{C}(\lambda_m) \mathbf{v}_m \mathbf{w}_m^H \mathbf{B}(\lambda_m)}{-\mathbf{w}_m^H \mathbf{A} \mathbf{T}'_a(\lambda_m) \mathbf{v}_m}. \quad (13)$$

This is the outer product of two vectors (and a scalar):

$$\mathbf{R}_m = \rho_{c,m} \rho_{b,m}^H \rho_{a,m}, \quad (14)$$

where

$$\rho_{a,m} = \frac{1}{-\mathbf{w}_m^H \mathbf{A} \mathbf{T}'_a(\lambda_m) \mathbf{v}_m}, \quad (15a)$$

$$\rho_{b,m}^H = \mathbf{w}_m^H \mathbf{B}(\lambda_m), \quad (15b)$$

$$\rho_{c,m} = \mathbf{C}(\lambda_m) \mathbf{v}_m. \quad (15c)$$

These terms’ dependency (or lack thereof) on the input-output parameters is noteworthy – that is to say, the fact that $\rho_{b,m}$

exclusively depends on input parameters ($\mathbf{B}(z)$), and $\rho_{c,m}$ exclusively depends on output parameters ($\mathbf{C}(z)$). In fact, there is a total separation of individual sound sources and individual listeners; each source only affects one element of $\rho_{b,m}$, and each listener one element of $\rho_{c,m}$. The scalar term $\rho_{a,m}$ is the undriven residue [26], and as its name implies it is independent of the input-output parameters. This separation has considerable repercussions on computational complexity, discussed in Section IV. In terms of physical significance, the form of (14) implies that each mode's positional dependence can be encapsulated into one complex scalar for each sound source, and one complex scalar for each listener.

The left and right eigenvectors \mathbf{w}_m and \mathbf{v}_m also appear separately in $\rho_{b,m}$ and $\rho_{c,m}$. This reveals the eigenvectors' nature as the input-output coupling of each mode. Consider the matrix multiplications in (15b) and (15c): the eigenvectors translate spatial energy distributions into modal excitations.

3) *Sample rate and fractional delays*: It is worth taking a moment to discuss the values of the time delays in $\mathbf{T}_a(z)$, which model propagation times throughout the environment. The correct modeling of reverberation, of course, relies on these propagation times being captured accurately. Since TD-ART is a digital filter, working in discrete time, its operation requires discrete delay lengths. Fractional delay filters would introduce negative values, making their use in ART problematic (the propagated signals are energy quantities, and negative values are not permitted); therefore, the delay lengths must be integer. When TD-ART is run conventionally, this causes a trade-off concerning the echogram sample rate: low sample rates increase the rounding error in these integer delays, while high sample rates increase the computational cost of running the system (see Section IV-C).

When it comes to MoD-ART, the same trade-off takes on a different form. The modal decomposition approaches TD-ART analytically, and one can analyze a TD-ART model as if it used ideal fractional delays. This is only possible with one of the two decomposition approaches presented in the following section. With fractional delays, rounding error is no longer a concern, and the sample rate may be arbitrarily low; the trade-off is the temporal resolution of the modeled echogram. Unfortunately, as discussed in Section IV-B, the decomposition approach which enables the use of ideal fractional delays is considerably more computationally expensive than the one which does not. The effects that the sample rate has on poles are illustrated and discussed further in Section V-C.

B. Reduced mode selection

Based on the physical significance of the modal parameters, it can be deduced that a small number P of modes is sufficient to model late reverberation. Specifically, the required modes can be selected based on two criteria, presented here. Both criteria stem from the specific focus of MoD-ART on late reverberation, i.e., the assumption is that the earliest portion of the echogram is modeled through other means.

The first criterion concerns poles' magnitudes, related to modes' reverberation times by (11). Since modes are characterized by exponential decay, when the echogram reaches late

reverberation the faster-decaying modes are many orders of magnitude smaller than the slower-decaying ones. As such, small poles have negligible influence on late reverberation – the first selection criterion disregards all poles below some given magnitude threshold. The chosen magnitude threshold dictates the decay time threshold T_d after which the reduced decomposition gives an accurate approximation of the echogram – the implications of this choice with regards to complexity are discussed in Section IV-B. If T_d is low, more poles are included in the selection, and the earlier part of the echogram is captured more accurately. If T_d is high, fewer poles are included in the selection, prioritizing the later part of the echogram.

The second criterion concerns poles' phases, related to modes' frequencies by (12). In most late reverberation modeling scenarios, one is only interested in modeling the non-oscillatory energy decay modes – i.e. only the real, positive poles are required. In cases where more detailed late energy dynamics are desired, e.g. if flutter echoes are expected, (12) may inform the selection of modes with different periods.

In the following, we discuss two techniques to obtain the poles; their advantages, disadvantages, and use cases.

1) *Ehrlich-Aberth iteration*: The first pole-finding technique we present here is Ehrlich-Aberth iteration (EAI), as adapted by Schlecht and Habets [26]. This approach was developed for systems with the same form as (1), although the system in [26] was not restricted to positive values (it was not an energy model). The pole search starts from M initial estimates $\lambda_m^{(0)}$, $m \in 1, \dots, M$, spaced uniformly on the unit circle. Each estimate is then iteratively updated as

$$\lambda_m^{(i+1)} = \lambda_m^{(i)} - \Delta_m^{(i)}, \quad (16)$$

where the correction term $\Delta_m^{(i)}$ is a combination of the common Newton step (as utilized in the Newton root-finding method [29]) and a deflation term, which penalizes pairs of estimates in close proximity – i.e. it prevents multiple estimates from converging to the same solution. It bears mentioning that the Newton step requires a matrix inversion, $\mathbf{P}^{-1}(\lambda_m^{(i)})$; this will be relevant to the method's computational complexity, discussed in Section IV-B. We refer to [26] for a full discussion of these terms and the overall process.

The iteration as carried out in [26] aims to achieve a full decomposition (i.e. finding all M poles), and as such, it terminates on convergence of all estimates. Convergence is assessed based on two criteria: if the latest step $|\lambda_m^{(i)} - \lambda_m^{(i-1)}|$ is smaller than some threshold, and/or if the condition number $\kappa(\mathbf{P}(\lambda_m^{(i)}))$ is larger than some threshold, the estimate $\lambda_m^{(i)}$ is no longer updated. For our purposes, as previously discussed, a full decomposition is not desired – only poles with significant magnitude are sought. As such, we introduce a third stopping criterion: iteration is halted when estimates fall below a magnitude threshold. From (11),

$$\left| \lambda_m^{(i)} \right| < 10^{-\frac{6}{T_d f_s}}, \quad (17)$$

where T_d is the desired time threshold, as discussed above.

An interesting aspect of the EAI approach is that it finds the roots of the polynomial (5) even if the polynomial describes a

filter that cannot be implemented in practice, such as one involving noncausal or ideally fractional delays. Performing the decomposition with ideally fractional delays is a feature with multiple advantages, discussed in further detail in Section V-C.

2) *Arnoldi iteration*: The system poles may also be found as eigenvalues of the state transition matrix, detailed in Appendix A. Unlike EAI, this approach precludes the use of ideal fractional delays in the analysis, because constructing the state transition matrix is only possible if the propagation delays are integer. Furthermore, the eigenvalue decomposition cannot be exclusively targeted to the real axis, making this approach less fitting in cases where oscillatory modes are irrelevant. Nevertheless, this approach is worth mentioning here, because of its higher efficiency. Thanks to the very high sparsity of the state transition matrix and to the fact that only a few eigenvalues are desired, the decomposition can be performed using the Arnoldi iteration method [30]. The comparative computational complexity of this approach with respect to EAI is discussed further in the following section.

IV. COMPUTATIONAL COMPLEXITY

The computational costs of MoD-ART can be differentiated between precomputation (offline) and interactive (runtime) components, as listed at the start of Section III. Since MoD-ART is intended for real-time interactive applications, where runtime efficiency is paramount, this section prioritizes the discussion of interactive elements. Some aspects of the precomputation are also briefly discussed, but a more extensive analysis is left for future works. Moreover, we do not account for costs which are common between our method and other modeling approaches, e.g. the cost of noise-shaping, the cost of convolution, and the process's repeated application for different frequency bands.

A. Evaluation of EAI

The ART matrix \mathbf{A} can be found by analytical means in some situations [31], but it is usually evaluated through ray-tracing [15]. The leading factor in the complexity of ART, and by extension of MoD-ART, is the number of volumetric paths N . This is related to the number of discrete surface patches and to the geometrical complexity of the environment. Let us say, for example, that each of the N_{Polys} polygons making up the environment mesh is taken to be a discrete surface patch, and that each one (on average) has visibility on $V N_{\text{Polys}}$ other polygons, with $0 < V < 1$. Then, the number of volumetric paths is $N = N_{\text{Polys}}(V N_{\text{Polys}})$, because paths only exist between mutually visible surface patches. The value V is low when the environment is highly geometrically complex, and can only equal 1 if each surface patch has visibility on all surface patches – meaning the enclosure is strictly convex, and surface patches have self-visibility (impossible when they are planar polygons). Consider, for example, an environment with 10 rooms of 100 polygons each ($N_{\text{Polys}} = 1000$), such that each polygon (on average) has visibility on roughly 100 polygons in the same room and 20 polygons from adjacent rooms. Then, we have a visibility ratio of $V = 120/1000 = 0.12$, and $N = 1000 \cdot 120 = 1.2 \cdot 10^5$ volumetric paths.

In many cases, the environment mesh features a high number of small polygons. For the purpose of ART, it is desirable to have fewer, larger patches, to reduce the runtime complexity at the cost of a slightly coarser approximation. Reducing the polygon count of the environment mesh is possible to some extent [32], but some important features of the space may be lost in doing so. Another option is to define discrete surface patches which span several adjacent polygons, possibly allowing non-planar surface patches. This approach has the potential to greatly decrease the size N of the ART matrix, and therefore the computational complexity of the modal decomposition and of the runtime elements. In the following, to avoid confusion, we maintain the assumption of each patch being a single polygons, and use N_{Polys} to denote the number of discrete surface patches.

Another crucial factor in the complexity of ART is the number of nonzero elements of \mathbf{A} , which is a very sparse matrix. The sparsity of \mathbf{A} is due to the fact that it only describes valid reflections. Take for example a path connecting two surface patches a and b : the energy traversing this path will be reflected by b , therefore it may only be redirected to paths that start from b . Let us say, as before, that $V N_{\text{Polys}}$ is the number of paths starting from any given surface patch; the number of nonzero elements of \mathbf{A} is then $N(V N_{\text{Polys}})$, i.e. $N_{\text{Polys}}(V N_{\text{Polys}})^2$. This corresponds to just a fraction $1/N_{\text{Polys}}$ of the total number of elements (including zeros) of \mathbf{A} , which is $N^2 = N_{\text{Polys}}^2(V N_{\text{Polys}})^2$.

B. Modal decomposition

The bulk of decomposition costs relates to finding the poles, rather than the eigenvectors, which are found from the adjugate² once the poles are known. Here, we briefly compare the two pole-finding techniques presented in Section III-B, in terms of computational complexity.

1) *EAI approach*: The crux of EAI's complexity lies in the matrix inversion required by the Newton step, for each estimate, at each iteration. Unlike other parts of the iterative process, matrix inversion cannot benefit from the sparse nature of the matrix $\mathbf{P}(z)$. In addition to this, the process must start with all M estimates (i.e. as many as the system order) in order for the deflation process to work as intended. As such, the complexity of a single iteration (updating all estimates) is

$$O(M^2 + MN^3) . \quad (18)$$

Further details are given in [26]. The system order M is always larger than the number of paths N , but (in TD-ART models) the term MN^3 is usually much larger than M^2 .

2) *Arnoldi approach*: The Arnoldi iteration method for eigenvalue decomposition has two main advantages, in terms of efficiency: it allows searching for a small subset of eigenvalues, and it exploits matrix sparsity [30]. The subset of eigenvalues can be selected through different priority criteria, such as larger or smaller amplitude [33]; as with the EAI approach, the search can be halted when the desired magnitude threshold is reached. The leading term in the computational complexity

²Since the adjugate is the outer product of the eigenvectors (see (8)), they are easily derived from the first row and first column of the adjugate.

of Arnoldi iteration is related to a matrix-vector multiplication between the matrix to be decomposed (in this case, the state transition matrix) and a candidate eigenvector [33]. The cost of such a multiplication is proportional to the number of nonzero elements in the matrix. For a dense matrix, this would be the square of its size. The state transition matrix, however, is exceedingly sparse: despite having a size of $M \times M$, its nonzero elements are $(M - N)$ plus the nonzero elements of \mathbf{A} (see Appendix A). As previously stated, \mathbf{A} has $N(VN_{\text{Polys}})$ nonzero elements, and as such, the state transition matrix has $M - N + N(VN_{\text{Polys}})$ nonzero elements. In conclusion, if P poles are desired, the complexity of the Arnoldi approach is

$$O(P(M + N(VN_{\text{Polys}} - 1))) . \quad (19)$$

C. Interactive elements

In the following, we assume that all non-interactive parameters (i.e. poles λ_m , eigenvectors \mathbf{w}_m , \mathbf{v}_m , and undriven residues $\rho_{a,m}$) have been precomputed. What remains to be done is evaluating the input-output parameters $\mathbf{B}(z)$, $\mathbf{C}(z)$ and the residues \mathbf{R}_m . This process may be repeated at fixed intervals, or only upon movement of the sources/listeners.

1) *Ray-tracing*: As introduced in Section II-A, the input-output parameters of ART are evaluated through a single order of ray-tracing from each source, and from each listener. For the sake of comparison against a full RTM approach, let us discuss the complexity of ray-tracing for an arbitrary reflection order N_{Ref} . In a “naive” implementation of the method, each of the L listeners casts N_{Rays} rays, and each ray (at each reflection) checks for intersections with all objects: N_{Polys} polygons, and S sources (spherical interceptors). In short, the complexity is

$$O(LN_{\text{Ref}}N_{\text{Rays}}(N_{\text{Polys}} + S)) . \quad (20)$$

In optimized RTM implementations such as KD-Tree traversal [34], polygons are organized into a structure that greatly expedites the intersection process, and the complexity becomes

$$O(LN_{\text{Ref}}N_{\text{Rays}}(\log(N_{\text{Polys}}) + S)) . \quad (21)$$

Note that, if any of the sources move, the tracing process needs to be re-run from all listener positions. If all sources are static and some listeners move, the process needs to be re-run only for moving listeners. On the contrary, for the purpose of computing $\mathbf{B}(z)$ and $\mathbf{C}(z)$ for ART, all sources and listeners are independent: if a single source or listener moves, only the parameters related to that individual need to be updated. The tracing process then only needs to be performed from the positions of recently moved sources/listeners, with the complexity of a single order of ray-tracing from each position:

$$O(\hat{S}N_{\text{Rays}} \log(N_{\text{Polys}}) + \hat{L}N_{\text{Rays}} \log(N_{\text{Polys}})) , \quad (22)$$

where \hat{S} and \hat{L} refer to the number of sources and listeners which have moved since the last update, respectively. This is equivalent to performing (21) from each new position, with $N_{\text{Ref}} = 1$, and without considering intersections with sources.

2) *Running TD-ART*: The standard operation of TD-ART, once its parameters have been prepared, is equivalent to running the digital filter described by (1). The main cost is that of the matrix-vector multiplication $\mathbf{A}\mathbf{s}$, which has complexity $O(NVN_{\text{Polys}})$ – the number of nonzero elements in \mathbf{A} , as previously discussed. In addition to this, there are the multiplications with \mathbf{B} and \mathbf{C} , which are also sparse. Indeed, like \mathbf{A} , the input-output operators \mathbf{B} and \mathbf{C} are also affected by the visibility parameter V . As previously stated, only VN_{Polys} polygons are visible (on average) from any given position in the environment. If a sound source has visibility on VN_{Polys} surface patches, then it can only contribute energy to the VN volumetric paths which start from those visible patches; equivalently, a listener can only detect energy from VN volumetric paths. As such, the number of nonzero elements in \mathbf{B} is SVN , and those in \mathbf{C} are LVN . In conclusion, the multiplications with \mathbf{B} and \mathbf{C} have complexity $O(SVN + LVN)$. All of these operations need to be performed for every sample of the echogram, making the overall complexity

$$O(N_{\text{Samples}}NV(S + L + N_{\text{Polys}})) , \quad (23)$$

where N_{Samples} is the length of the desired echogram.

Since TD-ART is a time-iterative process, all of the aforementioned matrix multiplications need to be performed for each time sample of the echogram. The time delays in $\mathbf{T}_a(z)$ and in each filter do not constitute a computational requirement in terms of operations, but in terms of memory space; there are two ways to handle them. The most common approach [18] is to instantiate a matrix of size $N \times N_{\text{Samples}}$, and use it to store the energy $\mathbf{s}(z)$ over time. The advantage of this approach is that, if listeners move but sound sources are static, only the multiplications with \mathbf{C} need to be performed interactively [17]. An alternative approach is to implement TD-ART as a filter similar to a Feedback Delay Network (FDN) [35]. This way, the iteration needs to be run interactively even if sources are static, but the memory requirements are reduced to the lengths of the propagation paths [36].

3) *Running MoD-ART*: The MoD-ART approach requires the computation of the input-output weights $\mathbf{B}(z)$ and $\mathbf{C}(z)$ with complexity (22), but it avoids the runtime cost (23). Once all ART parameters have been prepared (for P selected poles), the residue components $\rho_{b,m}$ and $\rho_{c,m}$ are computed with the dot products in (15), with complexity

$$O(PNV(\hat{S} + \hat{L})) . \quad (24)$$

The dot product in (14) is not required in practice, since the residue components can be stored and applied separately.

In addition to avoiding the time-iterative multiplications with \mathbf{A} , \mathbf{B} , and \mathbf{C} , MoD-ART also circumvents the memory requirements of TD-ART. The temporal evolution of modes is implicitly described by the poles, and the echogram’s reconstruction with (4) only requires enough memory to store the echogram itself. The eigenvectors \mathbf{w}_m , \mathbf{v}_m require memory equal to $2NP$ (two eigenvectors of size N for each mode). The individual elements of \mathbf{B} and \mathbf{C} can be evaluated and applied in (15b) and (15c) without allocating memory space for the

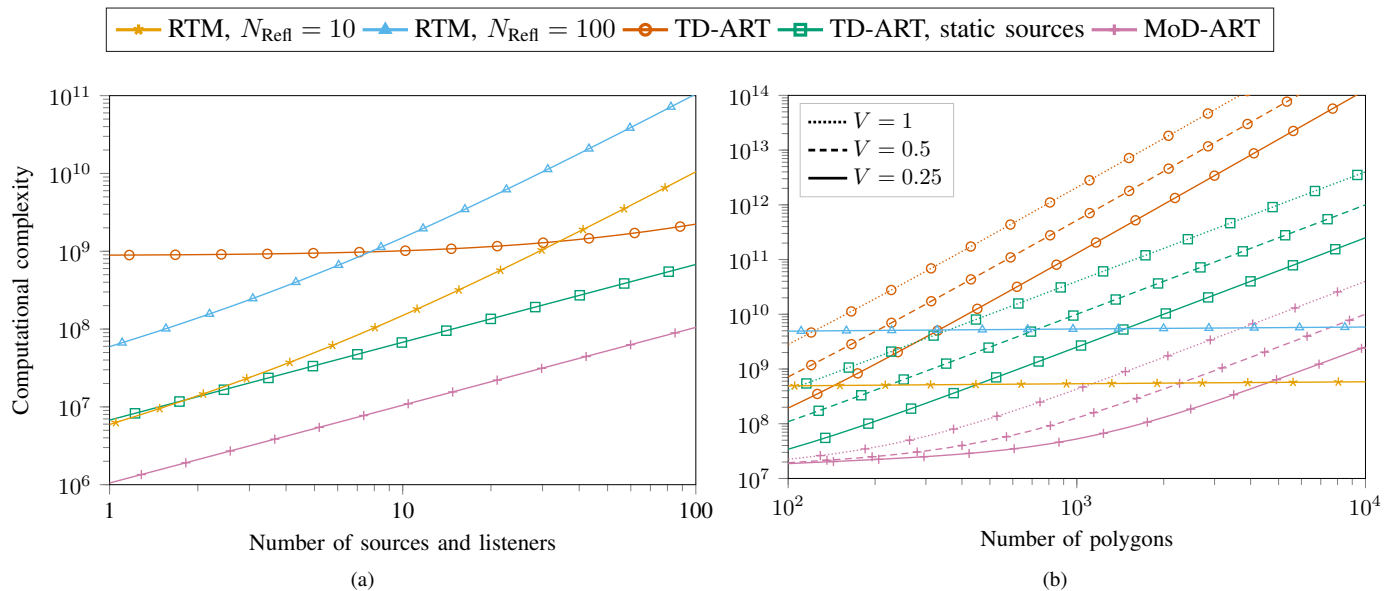


Fig. 4: Computational complexity comparison of RTM, TD-ART, and MoD-ART, as discussed in Section IV-D. All methods consider interactively updated source and listener positions, except for “TD-ART, static sources” where only listeners are updated. Complexity is plotted in (a) as a function of sources and listeners, considering the three-room case shown in Fig. 5 in terms of numbers of polygons and visibility. In (b), complexity is plotted as a function of the number of polygons, in three hypothetical environments with different visibility factors: $V = 0.25$ (solid lines, low visibility), $V = 0.5$ (dashed lines, moderate visibility), and $V = 1$ (dotted lines, strictly convex enclosure).

entire matrices \mathbf{B} and \mathbf{C} , avoiding an additional memory requirement of $NV(S + L)$.

Finally, as the decomposition only provides the late reverberation, the computational cost of modeling the early echoes should be taken into account. That is to say, if accurate early reflections are desired, MoD-ART needs to be modified by adding two extra steps in the sequence presented at the start of Section III: model the early reflections using e.g. beam-tracing or ray-tracing (very small N_{Ref}), and splice the early and late echograms together. If RTM is chosen to do this, some operations may be saved by performing this at the same time as the ray-tracing for \mathbf{B} and \mathbf{C} .

D. Comparisons

To summarize, in a scenario where all sources and listeners may move interactively, the runtime computational complexity (in terms of operations) of RTM is given by (21), that of TD-ART is the sum of (22) and (23), and that of MoD-ART is the sum of (22) and (24). If the sound sources’ positions are fixed, (23) may be reduced to $O(N_{\text{Samples}}NVL)$ at the expense of memory space. These costs are compared in Fig. 4. For simplicity, we consider the same number of sources and listeners ($S = L$), and assume that all of them are updated at every opportunity ($\hat{S} = S$, $\hat{L} = L$). The plots in Fig. 4 include two versions of RTM: one with a low reflection order $N_{\text{Ref}} = 10$, which can only capture early reflections; one with a higher reflection order $N_{\text{Ref}} = 100$, more suitable for late reverberation modeling. These are compared with TD-ART and MoD-ART, as well as the special case of TD-ART where all sources are static. In both plots of Fig. 4, we consider

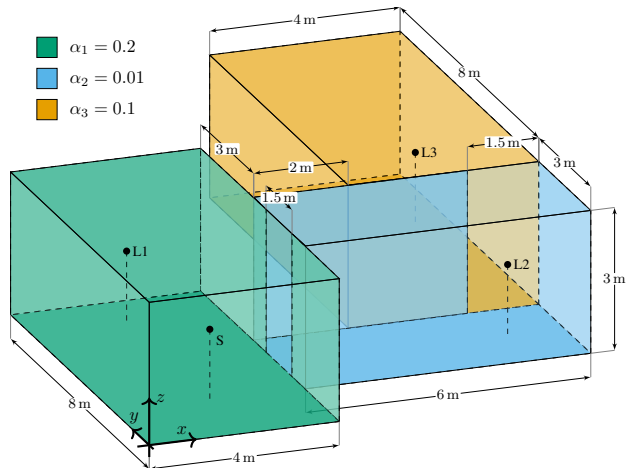


Fig. 5: The environment used in the presented tests. Source and listener positions are also reported in Table I.

$N_{\text{Rays}} = 10^5$ rays, $N_{\text{Samples}} = 2000$ echogram samples (two seconds at 1 kHz), and $P = 10$ slopes.

In Fig. 4a, each method’s computational complexity is shown as a function of the number of sources and listeners. For this plot, we consider the geometry shown in Fig. 5, which is also used for the simulation results in the next section. The scene has $N_{\text{Polys}} = 140$ surface patches and $N = 7982$ volumetric paths, implying a visibility factor of $V \approx 0.4$. With these parameters, TD-ART is more computationally expensive than RTM when the number of interactive elements is low, but becomes preferable with ten or more sources and listeners. In the special case with static sources, TD-ART is always

TABLE I: Source and listener positions used in the presented tests. These are also shown in Fig. 5.

	S	L1	L2	L3
x (m)	2.0	2.0	8.8	9.3
y (m)	2.0	6.8	3.5	10.2
z (m)	1.5	1.5	1.5	1.5

more advantageous than RTM; in fact, it has lower complexity than even low-order RTM, while capturing late reverberation much more accurately. MoD-ART requires even fewer operations, as well as allowing the movement of sources and listeners both, and having much lower memory requirements than either TD-ART implementation. Overall, both TD-ART and MoD-ART scale better with the number of sources and listeners than RTM does.

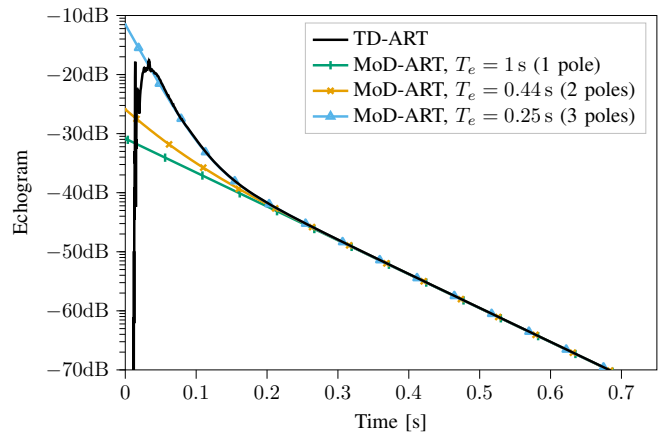
In Fig. 4b, the number of sources and listeners is fixed to $S = L = 20$, and complexity is shown as a function of the number of polygons. The complexity of TD-ART and MoD-ART is shown for three different levels of geometrical complexity of the environment: a case with moderate visibility ($V = 0.5$: each polygon has, on average, visibility on half of all polygons), a case with low visibility ($V = 0.25$: each polygon has, on average, visibility on a quarter of all polygons), and the case of a strictly convex enclosure ($V = 1$: each polygon has visibility on all polygons). The complexity of RTM is unaffected by the visibility factor. Note that having $V = 1$ is quite unlikely in environments of interest for our application: higher levels of geometrical complexity (i.e. lower values of V) are what lead to complex late reverberation behaviour, which MoD-ART is designed for. Moreover, note that the upper limit of $N_{\text{Polys}} = 10^4$ polygons on the axis of Fig. 4b is very high in the context of room acoustics modeling [32]. Due to the logarithmic complexity scaling of ray-tracing with respect to the number of polygons, RTM is much more efficient than either implementation of TD-ART when the environment's polygon count is moderate-to-high. Fully interactive TD-ART is only preferable to RTM in scenarios with low polygon counts and high geometrical complexity. In contrast, MoD-ART is in most cases more efficient than even low-order RTM, and only surpasses the complexity of high-order RTM in the worst-case scenarios with very high polygon counts and very low geometrical complexity.

V. RESULTS

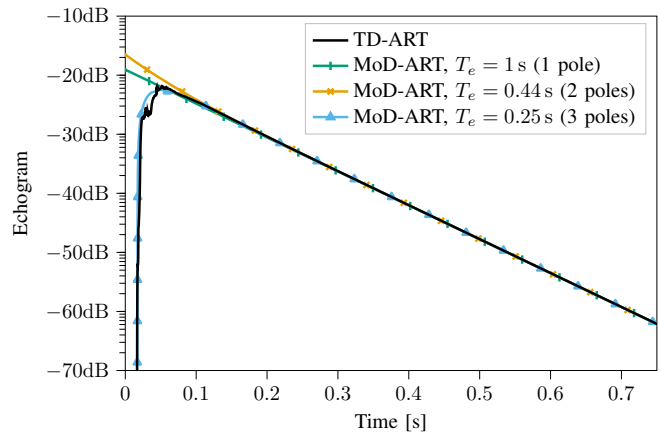
This section demonstrates different aspects of the proposed method. The correspondence between real, positive poles and energy decay slopes is illustrated, and the selection of modes based on their magnitude is justified, in Section V-A. One possible use case for complex poles is presented in Section V-B, where they are used to characterise a flutter echo. Lastly, Section V-C illustrates the effects of different echogram sample rates and fractional delays on the decomposition.

A. Slopes and decay time threshold

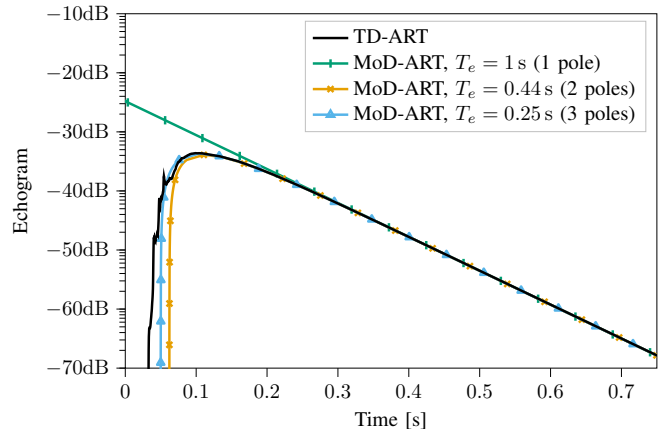
The connection between energy decay slopes and real, positive poles of ART is validated by considering a coupled-volume environment comprising three rooms, shown in Fig. 5.



(a) Listener L1



(b) Listener L2



(c) Listener L3

Fig. 6: Echograms for the three listener positions in Fig. 5, modeled with TD-ART and MoD-ART. Results of the proposed method are shown for three different values of T_d , using only real, positive poles in all cases.

The three rooms have absorption coefficients (from left to right) $\alpha_1 = 0.2$, $\alpha_2 = 0.01$, and $\alpha_3 = 0.1$, i.e. the middle room is more reverberant than the side rooms. The plots in Fig. 6 show echogram comparisons for three different positions of the listener, given one position of the sound source. The source

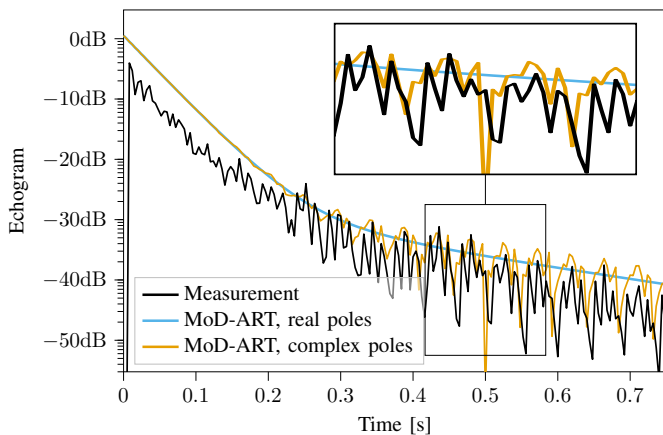


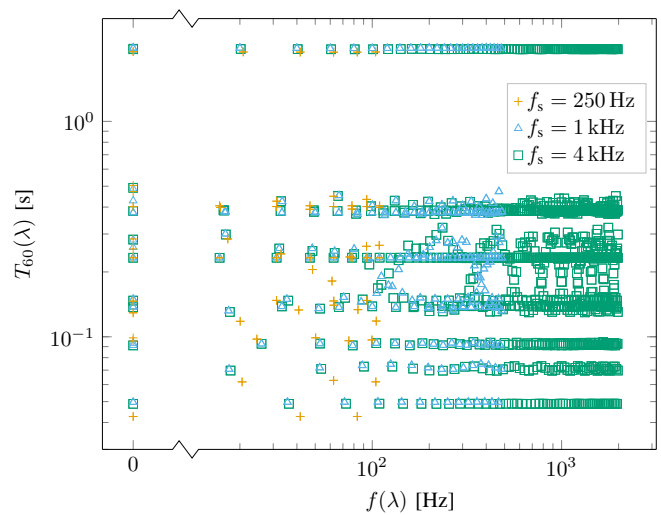
Fig. 7: Echogram of a measurement from the Arni dataset [37] and two decompositions using the proposed approach, with or without complex poles. Complex poles capture the flutter echo in the environment, while the decomposition restricted to real, positive poles cannot model the oscillatory phenomenon.

and listener positions are reported in Table I, and included in Fig. 5. The modal decomposition was performed with the Arnoldi approach, using an echogram sample rate of 4 kHz.

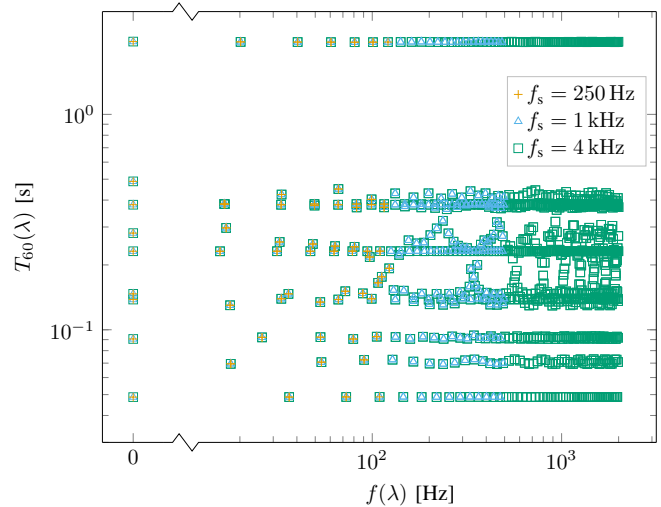
The results of the decomposition are shown for three different values of the decay time threshold T_d , selecting only real, positive poles in all cases. Decreasing T_d – i.e. including more poles in the decomposition – gradually increases the accuracy of the result. Specifically, including poles in decreasing order of magnitude prioritizes the accuracy of the late reverberation, gradually decreasing the time threshold after which the approximation is acceptable. Note that Fig. 6b and 6c show a gradual fade-in of the response, due to the sound source and listener being located in different rooms [28]. This is reflected by the signs of slopes in the decomposition – negative slopes detract energy from the echogram. Note how the signs of the slopes in Fig. 6 match those of residues in Fig. 3, given the listeners’ positions: the third-most reverberant mode is negative for L2, and the second-most is negative for L3.

B. Complex poles

The significance of complex poles was validated by modeling a flutter echo. A measurement from the Arni variable acoustics room dataset [37] was considered – specifically, one using panel configuration 8, known to produce a flutter echo [38]. The room was modeled as a simple shoebox, divided into $N_{\text{Polys}} = 32$ surface patches, which resulted in $N = 848$ volumetric paths. The modal decomposition was performed with an echogram sample rate of 250 Hz, using the EAI approach and ideal fractional delays. In Fig. 7, two different decomposition results are compared to the measured echogram. Both decompositions use decay time threshold $T_d = 0.3$ s; one uses only real, positive poles, and the other uses all (complex) poles. As expected, the decomposition limited to real, positive poles only includes non-oscillatory modes, and therefore fails to capture the flutter. On the contrary, the complex poles correctly capture the flutter.



(a) Integer delays



(b) Fractional delays

Fig. 8: Modal decompositions using different echogram sample rates f_s , with integer (a) or fractional (b) delays. Axes show modes’ T_{60} and frequency as defined in (11), (12). Note that modes never surpass the Nyquist frequency related to f_s .

Note that the prediction of flutter echoes is no trivial task, especially ones that carry on throughout late reverberation. Past approaches have relied on wave-based simulations, or RTM simulations with very high fidelity [39]. In order to capture a long flutter echo reliably using ray-tracing, one needs to use a high reflection order and a very high number of rays. This is because low numbers of rays and approximate scattering models lead to errors which worsen with increasing reflection orders [40]. Acoustic Radiance Transfer does not suffer from such errors, since its parameters inherently model the environmental characteristics which cause the flutter echo. It follows that the same can be said of MoD-ART.

C. Sample rate and fractional delays

The effects of different sample rates on poles, previously discussed in Section III-A3, are illustrated in Fig. 8. These

plots are produced by running the decomposition for different sample rates, with integer or fractional delays, having fixed \mathbf{A} and the propagation distances. The plotted quantities are the T_{60} and frequency of the poles – see (11) and (12).

The first observation to be made is that, predictably, fractional delays prevent the rounding error issue entirely. It can be seen from Fig. 8a that, when integer delays are used, changing the sample rate leads to changes in the resulting modes – as previously stated, the behaviour captured with higher sample rates is the physically correct one. On the contrary, as seen in Fig. 8b, changing the sample rate when fractional delays are used does not cause any change in the modes. In fact, as the sample rate increases, the values found with integer delays converge to the ones found with fractional delays, which further highlights how these are the correct values.

A second observation is that, for any given sample rate, one may only find modes up to the relative Nyquist frequency. As a result, if it is desired to model oscillatory behaviour (i.e. complex poles are to be accounted for), the sample rate needs to be set high enough to capture the highest oscillation frequency to be modeled – which, of course, increases the number of poles and the overall complexity of the approach. In order to capture the fundamental frequency of the flutter echo in Fig. 7, for example, the sample rate has to be at least 50 Hz. If, however, it is only desired to model non-oscillatory modes (i.e. only real, positive poles are to be accounted for), then the sample rate may be set arbitrarily low – which is only feasible with fractional delays, due to the rounding errors caused by integer delays.

VI. CONCLUSIONS

In this paper, we proposed a novel approach to model late reverberation at interactive speeds with complex geometries, including situations such as coupled volumes. The proposed method, named modal decomposition of Acoustic Radiance Transfer (MoD-ART), is highly suitable for applications with positionally dependent late reverberation, as well as multiple sound sources and/or listeners being able to move freely. By approaching Time-Domain Acoustic Radiance Transfer (TD-ART) as a digital filter, the salient energy decay modes of the modeled environment can be found in the form of system poles and residues. This modal decomposition provides a compact representation of the positional dependence of late reverberation, which can then be applied efficiently, requiring minimal computations at runtime. The proposed method is more efficient than both ray-tracing and TD-ART, as well as requiring considerably less memory space than TD-ART.

We presented different criteria for the selection of the most salient energy decay modes, depending on the circumstance. We showed that said selection may be scaled in favor of efficiency or accuracy; late reverberation is always prioritized, and early reverberation may also be modeled accurately (with a flexible decay time threshold) through the selection of additional modes. We also showed that the proposed method is able to capture periodic phenomena such as flutter echoes, providing accurate modeling throughout the late reverberation.

Future work could investigate how to implement the proposed decomposition method through a set of reverberators,

shared between all sources and listeners, to remove the cost of convolution.

APPENDIX A: STATE-SPACE REPRESENTATION

The TD-ART state equations (1) may be equivalently expressed in the “expanded” form

$$\mathfrak{s}(z) = \mathfrak{A}z^{-1}\mathfrak{s}(z) + \mathfrak{B}\mathbf{B}(z)\mathbf{x}(z), \quad (25a)$$

$$\mathbf{y}(z) = \mathbf{C}(z)\mathfrak{C}\mathfrak{s}(z) + \mathbf{D}(z)\mathbf{x}(z), \quad (25b)$$

where $\mathfrak{s} \in \mathbb{C}^{M \times 1}$ is the state vector (the “flattened” content of the propagation lines), $\mathfrak{A} \in \mathbb{R}^{M \times M}$ is the state transition matrix (defined in the following, in (28)), and

$$\mathfrak{B} = \begin{bmatrix} \mathbf{0} \\ \mathbf{I} \end{bmatrix} \in \mathbb{R}^{M \times N}, \quad \mathfrak{C} = [\mathbf{0} \quad \mathbf{I}] \in \mathbb{R}^{N \times M}. \quad (26)$$

Note that, in (25), the delay elements of $\mathbf{B}(z)$, $\mathbf{C}(z)$, and $\mathbf{D}(z)$ are left implicit, such that \mathfrak{s} only includes the state variables related to recursive delay lines (inside the feedback loop). The state transition matrix \mathfrak{A} describes the propagation of signals within the recursion loop: in other words, it describes the joint operation of both $\mathbf{T}_a(z)$ and \mathbf{A} in (1). In a “true” state-space representation, \mathfrak{s} would also include the state variables related to delay lines outside of the loop. The “partial” state-space representation in (25) is chosen for simplicity, since describing the non-recursive state variables explicitly would introduce needless complexity in these equations. The structures of \mathfrak{A} , \mathfrak{B} , and \mathfrak{C} are chosen such that the last N elements of \mathfrak{s} correspond to the vector \mathbf{s} from (1). If the propagation modeled by the diagonal matrix $\mathbf{T}_a(z)$ does not include temporal spreading, the elements of $\mathbf{T}_a(z)$ are

$$\text{diag}(\mathbf{T}_a(z)) = [z^{-\tau_{a,1}}, z^{-\tau_{a,2}}, \dots, z^{-\tau_{a,N}}], \quad (27)$$

where τ_a are the delay line lengths. The structure of \mathfrak{A} is:

$$\mathfrak{A} = \begin{bmatrix} \mathbf{E}_1 & \mathbf{0} & \mathbf{0} & \dots & \mathbf{0} & \mathbf{0} & \mathbf{F}_1 \\ \mathbf{0} & \mathbf{E}_2 & \mathbf{0} & \dots & \mathbf{0} & \mathbf{0} & \mathbf{F}_2 \\ \vdots & \vdots & \vdots & \ddots & \vdots & \vdots & \vdots \\ \mathbf{0} & \mathbf{0} & \mathbf{0} & \dots & \mathbf{E}_N & \mathbf{0} & \mathbf{F}_N \\ \mathbf{G}_1 & \mathbf{G}_2 & \mathbf{G}_3 & \dots & \mathbf{G}_N & \mathbf{0} & \mathbf{0} \\ \mathbf{0} & \mathbf{0} & \mathbf{0} & \dots & \mathbf{0} & \mathbf{A} & \mathbf{0} \end{bmatrix}, \quad (28)$$

where

$$\mathbf{E}_l = \begin{bmatrix} 0 & 1 & 0 & \dots & 0 \\ 0 & 0 & 1 & \dots & 0 \\ \vdots & \vdots & \vdots & \ddots & \vdots \\ 0 & 0 & 0 & \dots & 1 \\ 0 & 0 & 0 & \dots & 0 \end{bmatrix} \in \mathbb{R}^{(\tau_{a,l}-2) \times (\tau_{a,l}-2)}, \quad (29)$$

$$\mathbf{F}_l = \begin{bmatrix} 0 & \dots & 0 & 0 & 0 & \dots & 0 \\ 0 & \dots & 0 & 0 & 0 & \dots & 0 \\ \vdots & \ddots & \vdots & \vdots & \vdots & \ddots & \vdots \\ 0 & \dots & 0 & 0 & 0 & \dots & 0 \\ \underbrace{0 & \dots & 0 & 1 & 0 & \dots & 0}_{l-1} \end{bmatrix} \in \mathbb{R}^{(\tau_{a,l}-2) \times N}, \quad (30)$$

$$\mathbf{G}_l = \begin{bmatrix} 0 & 0 & \dots & 0 & 0 \\ \vdots & \vdots & \ddots & \vdots & \vdots \\ 0 & 0 & \dots & 0 & 0 \\ 1 & 0 & \dots & 0 & 0 \\ 0 & 0 & \dots & 0 & 0 \\ \vdots & \vdots & \ddots & \vdots & \vdots \\ 0 & 0 & \dots & 0 & 0 \end{bmatrix} \in \mathbb{R}^{N \times (\tau_{a,l}-2)}, \quad (31)$$

Note that \mathfrak{A} can only be defined when the propagation delays τ_a are integer, and also note that it is extremely sparse, containing a number of nonzero elements equal to $M - N$ plus the number of nonzero elements of \mathbf{A} . Lastly, an important feature of \mathfrak{A} is that its eigenvalues correspond to the poles of the TD-ART system [41].

APPENDIX B: DERIVATION OF $T_{60}(\lambda_m)$

Given an energy mode $e_m[n] = \rho_m \lambda_m^n$, consider its EDC

$$\text{EDC}[n] = \frac{\sum_{i=n}^{\infty} |\rho_m \lambda_m^i|}{\sum_{i=0}^{\infty} |\rho_m \lambda_m^i|} = \frac{\sum_{i=n}^{\infty} |\lambda_m^i|}{\sum_{i=0}^{\infty} |\lambda_m^i|}. \quad (32)$$

Note that the values are not squared, as the mode already describes energy. Replacing the geometric sums with their closed forms, we obtain $\text{EDC}[n] = |\lambda_m^n|$. The T_{60} is the time (measured in seconds) at which the EDC equals 10^{-6} . Since (32) is defined w.r.t. discrete time samples n , we have

$$\text{EDC}(T_{60}f_s) = |\lambda_m^{T_{60}f_s}| = 10^{-6} \quad (33)$$

$$T_{60}f_s = \log_{|\lambda_m|}(10^{-6}) = \frac{\ln 10^{-6}}{\ln |\lambda_m|}, \quad (34)$$

where f_s is the sample rate. Note that this derivation requires $|\lambda_m| \neq 1$: poles on the unit circle are critically stable, and have undefined T_{60} .

REFERENCES

- [1] M. Scerbo, S. J. Schlecht, R. Ali, L. Savioja, and E. De Sena, "A common-slopes late reverberation model based on acoustic radiance transfer," in *Proc. Int. Conf. on Digital Audio Effects (DAFx)*, DAFx, 2024, pp. 270–277.
- [2] T. Potter, Z. Cvetković, and E. De Sena, "On the relative importance of visual and spatial audio rendering on VR immersion," *Front. in Sig. Proc.*, vol. 2, pp. 904866, 2022.
- [3] Stefan Bilbao, "Modeling of complex geometries and boundary conditions in finite difference/finite volume time domain room acoustics simulation," *IEEE Trans. Audio, Speech, Language Proc.*, vol. 21, no. 7, pp. 1524–1533, 2013.
- [4] A. G. Prinn, "A review of finite element methods for room acoustics," in *Acoustics*, 2023, vol. 5(2), pp. 367–395.
- [5] S. Kirkup, "The boundary element method in acoustics: A survey," *Applied Sciences*, vol. 9, no. 8, pp. 1642, 2019.
- [6] B. Hamilton, *Finite difference and finite volume methods for wave-based modelling of room acoustics*, Ph.D. thesis, The University of Edinburgh, 2016.
- [7] J. B. Allen and D. A. Berkley, "Image method for efficiently simulating small-room acoustics," *J. Acoust. Soc. Amer.*, vol. 65, no. 4, pp. 943–950, 1979.
- [8] J. Borish, "Extension of the image model to arbitrary polyhedra," *J. Acoust. Soc. Amer.*, vol. 75, no. 6, pp. 1827–1836, 1984.
- [9] S. Laine, S. Siltanen, T. Lokki, and L. Savioja, "Accelerated beam tracing algorithm," *Applied Acoustics*, vol. 70, no. 1, pp. 172–181, 2009.
- [10] F. Antonacci, M. Foco, A. Sarti, and S. Tubaro, "Fast tracing of acoustic beams and paths through visibility lookup," *IEEE Trans. Audio, Speech, Language Proc.*, vol. 16, no. 4, pp. 812–824, 2008.
- [11] H. Kuttruff, *Room Acoustics, Fifth Edition*, CRC Press, 2009.
- [12] A. Krokstad, S. Strom, and S. Sørsdal, "Calculating the acoustical room response by the use of a ray tracing technique," *Journal of Sound and Vibration*, vol. 8, no. 1, pp. 118–125, 1968.
- [13] H. Autio, N.-G. Vardaxis, and D. B. Hagberg, "The influence of different scattering algorithms on room acoustic simulations in rectangular rooms," *Buildings*, vol. 11, no. 9, pp. 414, 2021.
- [14] L. Savioja and U. P. Svensson, "Overview of geometrical room acoustic modeling techniques," *J. Acoust. Soc. Amer.*, vol. 138, no. 2, pp. 708–730, 2015.
- [15] S. Siltanen, T. Lokki, S. Kiminki, and L. Savioja, "The room acoustic rendering equation," *J. Acoust. Soc. Amer.*, vol. 122, no. 3, pp. 1624–1635, 2007.
- [16] P. Luizard, J.-D. Polack, and B.F.G. Katz, "Sound energy decay in coupled spaces using a parametric analytical solution of a diffusion equation," *J. Acoust. Soc. Amer.*, vol. 135, no. 5, pp. 2765–2776, 2014.
- [17] S. Siltanen, T. Lokki, and L. Savioja, "Frequency domain acoustic radiance transfer for real-time auralization," *Acta Acustica united with Acustica*, vol. 95, no. 1, pp. 106–117, 2009.
- [18] S. Siltanen, T. Lokki, and L. Savioja, "Efficient acoustic radiance transfer method with time-dependent reflections," in *Proc. of Meetings on Acoustics*, 2011, vol. 12, p. 015007.
- [19] J. O. Smith, *Introduction to Digital Filters with Audio Applications*, <http://ccrma.stanford.edu/~jos/filters/>, accessed (10/03/2024), online book.
- [20] J. Botts and L. Savioja, "Spectral and pseudospectral properties of finite difference models used in audio and room acoustics," *IEEE/ACM Trans. Audio, Speech, Language Proc.*, vol. 22, no. 9, pp. 1403–1412, 2014.
- [21] Y. Haneda, Y. Kaneda, and N. Kitawaki, "Common-acoustical-pole and residue model and its application to spatial interpolation and extrapolation of a room transfer function," *IEEE Trans. Speech Audio Processing*, vol. 7, no. 6, pp. 709–717, 1999.
- [22] G. Götz, S. J. Schlecht, and V. Pulkki, "Common-slope modeling of late reverberation," *IEEE/ACM Trans. Audio, Speech, Language Proc.*, vol. 31, pp. 3945–3957, 2023.
- [23] M. Vorländer, *Auralization: Fundamentals of Acoustics, Modelling, Simulation, Algorithms and Acoustic Virtual Reality*, Springer, 2008.
- [24] Kuttruff K. H., "Auralization of impulse responses modeled on the basis of ray-tracing results," *J. Audio Eng. Soc.*, vol. 41, pp. 876–880, Nov. 1993.
- [25] J. M. Palmer and B. G. Grant, *Art of Radiometry*, Berlin: SPIE, 2010.
- [26] S. J. Schlecht and E. A. P. Habets, "Modal decomposition of feedback delay networks," *IEEE Trans. Signal Processing*, vol. 67, no. 20, pp. 5340–5351, 2019.
- [27] L. Farina and S. Rinaldi, *Positive linear systems: theory and applications*, vol. 50, John Wiley & Sons, 2000.
- [28] K. Y. Lee, N. Meyer-Kahlen, G. Götz, U. P. Svensson, S. J. Schlecht, and V. Välimäki, "Fade-in reverberation in multi-room environments using the common-slope model," *arXiv preprint arXiv:2407.13242*, 2024.
- [29] J.M. McNamee, "Numerical methods for roots of polynomials, part I," *Studies in Computational Mathematics*, vol. 14, 2007.
- [30] D. C. Sorensen, "Implicit application of polynomial filters in a k-step arnoldi method," *SIAM J. on matrix analysis and applications*, vol. 13, no. 1, pp. 357–385, 1992.
- [31] J. R. Howell and M. P. Mengüç, "Radiative transfer configuration factor catalog: A listing of relations for common geometries," *Journal of Quantitative Spectroscopy and Radiative Transfer*, vol. 112, no. 5, pp. 910–912, 2011.
- [32] S. Siltanen, T. Lokki, L. Savioja, and C. Lyngé Christensen, "Geometry reduction in room acoustics modeling," *Acta Acustica united with Acustica*, vol. 94, no. 3, pp. 410–418, 2008.
- [33] R. B. Lehoucq, D. C. Sorensen, and C. Yang, *ARPACK users' guide: solution of large-scale eigenvalue problems with implicitly restarted Arnoldi methods*, SIAM, 1998.
- [34] S. Popov, J. Günther, H. Seidel, and P. Slusallek, "Stackless KD-tree traversal for high performance GPU ray tracing," in *Computer Graphics Forum*, 2007, vol. 26, pp. 415–424.
- [35] J. M. Jot and A. Chaigne, "Digital delay networks for designing artificial reverberators," in *Proc. of the 90th Inter. Conf. of the Audio Eng. Soc.*, 1991, p. 3030.
- [36] M. R. Schroeder, "Natural sounding artificial reverberation," *J. Audio Eng. Soc.*, vol. 10, no. 3, pp. 219–223, 1961.
- [37] K. Prawda, S. J. Schlecht, and V. Välimäki, "Dataset of impulse responses from variable acoustics room arni at aalto acoustic labs," Zenodo. <https://doi.org/10.5281/zenodo.6985104>, Aug. 2022.
- [38] G. Del Santo, K. Prawda, and V. Välimäki, "Flutter echo modeling," in *Proc. Int. Conf. on Digital Audio Effects (DAFx)*, 2022, pp. 185–191.
- [39] H. Lai and B. Hamilton, "Computer modeling of barrel-vaulted sanctuary exhibiting flutter echo with comparison to measurements," in *Acoustics. MDPI*, 2020, vol. 2, pp. 87–109.
- [40] H. Lehnert, "Systematic errors of the ray-tracing algorithm," *Applied Acoustics*, vol. 38, no. 2-4, pp. 207–221, 1993.
- [41] D. Rocchesso and J. O. Smith, "Circulant and elliptic feedback delay networks for artificial reverberation," *IEEE Trans. Speech Audio Processing*, vol. 5, no. 1, pp. 51–63, 1997.